Estimating Effective Dose from Phantom Dose Measurements in Atrial Fibrillation Ablation Procedures and Comparison of MOSFET and TLD Detectors in a Small Animal Dosimetry Setting

by

Colin David Anderson-Evans

Graduate Program in Medical Physics
Duke University

Date: _____

Approved:

_____
Terry T. Yoshizumi, Supervisor

_____
Rathnayaka Gunasingha

_____
James Colsher

A thesis submitted in partial fulfillment of the
requirements for the degree of Master of
Science in the Graduate Program in Medical Physics
in the Graduate School
of Duke University

2011

ABSTRACT

Estimating Effective Dose from Phantom Dose Measurements in Atrial Fibrillation Ablation Procedures and Comparison of MOSFET and TLD Detectors in a Small Animal Dosimetry Setting

by

Colin David Anderson-Evans

Graduate Program in Medical Physics
Duke University

Date: _____

Approved:

_____
Terry T. Yoshizumi, Supervisor

_____
Rathnayaka Gunasingha

_____
James Colsher

An abstract of a thesis submitted in partial fulfillment of the requirements for the degree of Master of Science in the Graduate Program in Medical Physics in the Graduate School of Duke University
2011

Abstract

Two different studies will be presented in this work. The first involves the calculation of effective dose from a phantom study which simulates an atrial fibrillation (AF) ablation procedure. The second involves the validation of metal-oxide semiconducting field effect transistors (MOSFET) for small animal dosimetry applications as well as improved characterization of the animal irradiators on Duke University's campus.

Atrial Fibrillation is an ever increasing health risk in the United States. The most common type of cardiac arrhythmia, AF is associated with increased mortality and ischemic cerebrovascular events. Managing AF can include, among other treatments, an interventional procedure called catheter ablation. The procedure involves the use of biplane fluoroscopy during which a patient can be exposed to radiation for as much as two hours or more. The deleterious effects of radiation become a concern when dealing with long fluoroscopy times, and because the AF ablation procedure is elective, it makes relating the risks of radiation ever more essential.

This study hopes to quantify the risk through the derivation of dose conversion coefficients (DCCs) from the dose-area product (DAP) with the intent that DCCs can be used to provide estimates of effective dose (ED) for typical AF ablation procedures. A bi-plane fluoroscopic and angiographic system was used for the simulated AF ablation procedures. For acquisition of organ dose measurements, 20 diagnostic MOSFET detectors were placed at selected organs in a male anthropomorphic phantom, and these detectors were attached to 4 bias supplies to obtain organ dose readings. The DAP was recorded from the system console and independently validated with

an ionization chamber and radiochromic film. Bi-plane fluoroscopy was performed on the phantom for 10 minutes to acquire the dose rate for each organ, and the average clinical procedure time was multiplied by each organ dose rate to obtain individual organ doses. The effective dose was computed by summing the product of each organ dose and the corresponding tissue weighting factor from the ICRP publication 103. Further risk calculations were done according to the BEIR VII Phase 2 report to obtain relative and lifetime attributable risks of cancer for an average AF ablation procedure.

The ED was computed separately for the biplane fluoroscopic and angiographic system's 'low' and 'normal fluoro' automated settings, yielding 27.9 mSv and 45.6 mSv respectively for an average procedure time of 88.2 minutes. The corresponding DAP was 48.7 Gy cm^2 and 79.1 Gy cm^2 for low and normal settings respectively. The independently measured DAP was found to be within 0.1 % of that measured by the fluoroscopy system's onboard flat panel detectors. DCCs were calculated to be 0.573 and 0.577 for the respective low and normal settings. The results proved to be very closely matched, which was to be expected. The calculated cancer risks were fairly low due to the age of most patients (less than 5 incidences of solid tumor per 100,000 exposed for liver colon and stomach; 100-300 incidences per 100,000 exposed for lungs) , but concern remains that longer procedures could increase the risk of erythema or other serious skin injuries.

The second section of this thesis study involves the quantification and distribution of radiation dose in small animals undergoing irradiation in an orthovoltage x-ray unit. Extensive research is being done with small animals, particularly mice and rats, in fields such as cancer therapy, radiation biology and radiological countermeasures. Results and conclusion are often drawn from research based solely on manufacturer's specifications of the delivered dose rate

without independent verification or adequate understanding of the machines' capabilities. Accurate radiation dose information is paramount when conducting research in this arena.

Traditional methods of dosimetry, namely thermoluminescence dosimeters (TLDs) are challenging and often time consuming. This section hopes to show that in place of TLDs, MOSFETs can provide accurate, precise dose information comparable with TLDs and ionization chambers. Measurements of all three dosimeters are compared in a small animal irradiator in phantoms and in vivo. Measurements done with MOSFETs are shown to deviate by 2.5% from that of the ADCL calibrated ionization chamber while TLDs showed a 7% deviation. Dose distributions within a phantom is also measured using radiochromic film to estimate the attenuation and show that dose is not uniform throughout the mouse. A dose decrease of approximately 30% is observed in a water phantom, which was only slightly mitigated by a hardening the beam with additional filtration. A Bland-Altman plot was created to show that the MOSFETs and TLDs used to make the dose measurements are statistically equivalent. The results show that all measurements made over a range of doses fall within 1.96 standard deviations of the mean.

Table of Contents

List of Tables

List of Figures

Acknowledgments

I would like to acknowledge the support of Greta Toncheva for her help during experiments but most of all for keeping myself and all of our equipment organized; Samuel Brady for teaching me the appropriate use of radiochromic film; my advisor Terry Yoshizumi for his invaluable knowledge; and Dr. Thomas Wallace for his support and desire to see this research through without whom none of it would have been possible.

1 Introduction

Atrial fibrillation (AF), the most common cardiac arrhythmia, is a growing health risk in the US. AF is associated with increased mortality, hospitalizations, and ischemic cerebrovascular events. Management of AF includes a common procedure, utilizing the use of fluoroscopic imaging, known as catheter ablation (8). AF ablation procedures are of particular radiological concern due to the long exposure times associated with them. Because AF ablation procedures are elective, in that other treatment options are available, an assessment of the deleterious effects is warranted.

With the exception of some large scale radiological incidents and clinical treatment, direct research into human exposure to ionizing radiation is untenable. Small animals fill in as a proxy in radiation research and are used extensively to study radiation biology, cancer therapy efficacy, and medical countermeasures to radiological exposure. Fundamental to this research is the accurate measurement of absorbed dose to small animals. Inaccurate or imprecise measurements of dose can lead to incorrect conclusions about individual studies or dose-response relationships.

In order to draw valid conclusions from radiobiological studies, radiation dose must be quantitatively assessed in a precise manner. The following sections, 1.1 to 1.5, explain the physical quantities involved in dosimetry, describe several dosimeters and their methodologies, and describe the phantoms used to simulate actual clinical situations.

1.1 Physics Quantities

1.1.1 Exposure and Absorbed Dose

The effects of radiation on biological tissue are ultimately determined by the amount of energy absorbed in the tissue. This quantity, defined as energy absorbed per unit mass of the absorber, is

known as the radiation absorbed dose. Absorbed dose is measured in units of rad or gray (Gy) where

$$1\ Gy \overset{\text{def}}{=} \frac{1\ J}{kg} = \frac{10^7 erg}{10^3\ g} = 10^4 \frac{erg}{g} = 100\ rad \qquad (Equation\ 1.1)$$

The primary quantity measured in radiation dosimetry is exposure. For gamma or x-rays with less than 3 MeV of energy, exposure is defined as the amount of ionization produced in air. The International Commission on Radiological Units and Measurements (ICRU) gives the definition of exposure as:

$$X = \frac{\Delta Q}{\Delta m} \qquad (Equation\ 1.2)$$

where ΔQ is a sum of all charges of one sign produced by photons that are entirely stopped in the mass Δm of air. The unit, known as the roentgen, is thusly defined: 1 R = 2.58 X 10^{-4} C kg^{-1}. This concept is only applicable to photons ionizing air (Attix).

Measuring exposure without the express knowledge of each ionization produced by secondary electrons or delta rays originating in the target volume requires the establishment of charged particle equilibrium (CPE). CPE is said to exist when the fluence of charged particles entering or leaving a defined volume is equal. When CPE is established absorbed dose can be directly related to exposure by the relation:

$$D_{Air}\ (Gy) = X\left(\frac{C}{kg}\right) * \frac{\bar{W}}{e}\left(\frac{J}{C}\right) \quad or \quad D_{Air}\ (Gy) = 0.00869\left(\frac{Gy}{R}\right) * X\ (R) \quad (Equation\ 1.3)$$

Where D_{Air} is the absorbed dose to air in units of Gy, X is exposure in C/kg or R, and W/e is the energy necessary to produce one ion pair equal to 33.7 J/C. The conversion factor 0.00869 comes

from multiplying the definition of the roentgen with the energy necessary to create a single ion pair in air.

1.1.2 f-factors

In order to estimate dose to a given medium when measuring exposure in a defined volume of air contained within that medium, quantities known as f-factors must be employed. The ratio of the dose to the medium and air can be related via the ratio of their respective mass energy absorption coefficients (μ_{en}). In turn, the dose to the medium can then be related to the measured exposure giving the equation:

$$D_{med}(rad) = f * X(R) \qquad (Equation\ 1.4)$$

Here, f is the f-factor and is defined as:

$$f = 0.00869\left(\frac{Gy}{R}\right) * \frac{(\mu_{en})_{med}}{(\mu_{en})_{air}} \qquad (Equation\ 1.5)$$

Since the value of the f-factor is dependent on the mass energy absorption coefficient, it is therefore dependent on the energy of the radiation being considered as well as the nature of the absorbing medium.

1.1.3 Effective Dose

The International Commission on Radiological Protection (ICRP), along with other entities concerned with radiation protection, have introduced the concept of dose equivalent in order to discriminate between different types of radiations. The dose equivalent H is defined as the absorbed dose multiplied by a dimensionless factor Q. Q, known as the quality factor, is based on the biological effectiveness of different kinds of radiation, which in turn depends on the linear energy transfer (LET) of that particular radiation. LET is defined by the ICRP as the unrestricted

stopping power; in other words, the "average energy dE locally imparted to a medium by a charged particle traversing a distance dx".

$$LET = - (dE/dx) \qquad (Equation\ 1.6)$$

To account for the differing radiosensitivities of different tissues the ICRP further introduced the concept of effective dose. Along with the quality factor Q, the absorbed dose is multiplied by a tissue weighting factor (w_T) specific to the organ of interest. Since the sum of the ICRP's tissue weighting factors is unity, each individually weighted organ dose can be summed to obtain an effective dose that represents the risk for all stochastic effects to an irradiated individual. The equation is given by:

$$ED = \sum_T w_T H_T \qquad (Equation\ 1.7)$$

Where HT is the dose equivalent and the equivalent and effective doses are measured in units of Sieverts (Sv).

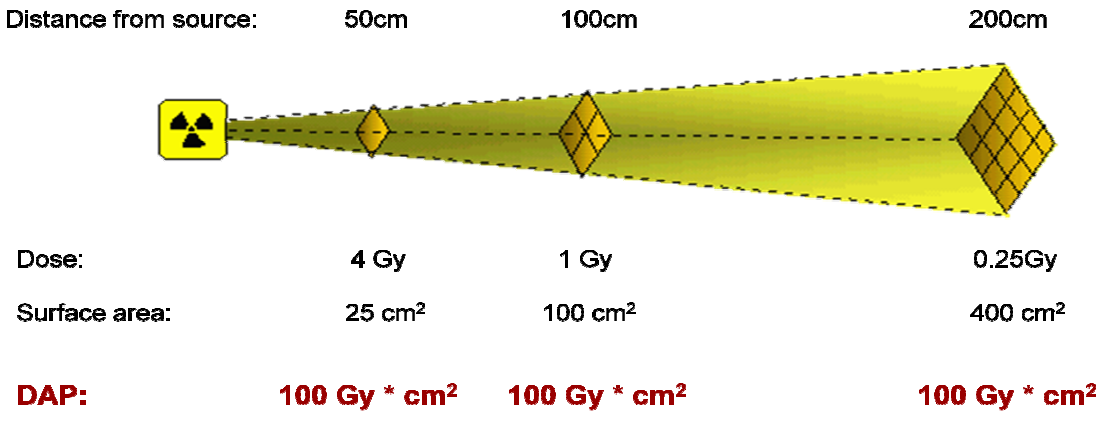

Figure 1. Illustration of DAP

1.1.4 Dose Area Product

Dose area product (DAP) is the product of the absorbed dose multiplied by the area of an x-ray beam centered at the point of measurement. It is primarily used in conjunction with radiography and interventional fluoroscopy so that a consistent dose value can be reported by the system for a given procedure. DAP is useful because it eliminates the inverse-squared dependency that dose has in relation to the distance (r) from the measurement point to the source of radiation. As illustrated in Figure 1, as the distance from the source increases, so does the area of the radiation field. Conversely, the dose will be reduced the further away the measurement point gets from the source, due to the same number of x-rays traversing a larger area and hence becoming more sparsely populated.

1.2 Dosimetry Methods

Dosimeters are a means of measuring the energy deposited in a particular medium. Dosimeters are categorized as absolute and relative, and involve different mechanisms to make dose measurements. Absolute dosimeters directly measure absorbed energy, either as heat in the material (known as calorimetry) or through measuring a chemical change caused by ionizing radiation. Calorimeters detect temperature rise by means of thermistors, while Fricke dosimeters typically measure the chemical change in ferrous sulfate. Relative dosimeters are required to be calibrated in a known radiation field in order to make accurate dose measurements. Relative dosimeters include ionization chambers and solid state detectors, ionization chambers being the most common method of dose measurement. Solid state detectors can be categorized as integrating or electrical conductivity dosimeters; the former includes thermoluminescence dosimeters (TLD), radiographic or radiochromic film, and dosimetric gels while the latter includes diodes, semiconductor junction detectors, and metal oxide semiconductor field effect

transistors (MOSFET). The techniques and detectors utilized in the ensuing work will be described in latter sections.

1.2.1 Ionization Chambers

Ionization chambers come in several configurations, the most common of which and those used for this work being of the cylindrical variety. On a fundamental level ionization chambers consist of a gas filled chamber that separates two electrodes used to collect opposite charges generated by ionizing radiation incident on the gas. For the case of cylindrical chambers an anode runs axially through the chamber with the outer wall acting as the cathode. A diagram of a simple cylindrical ionization chamber is shown in Figure 2.

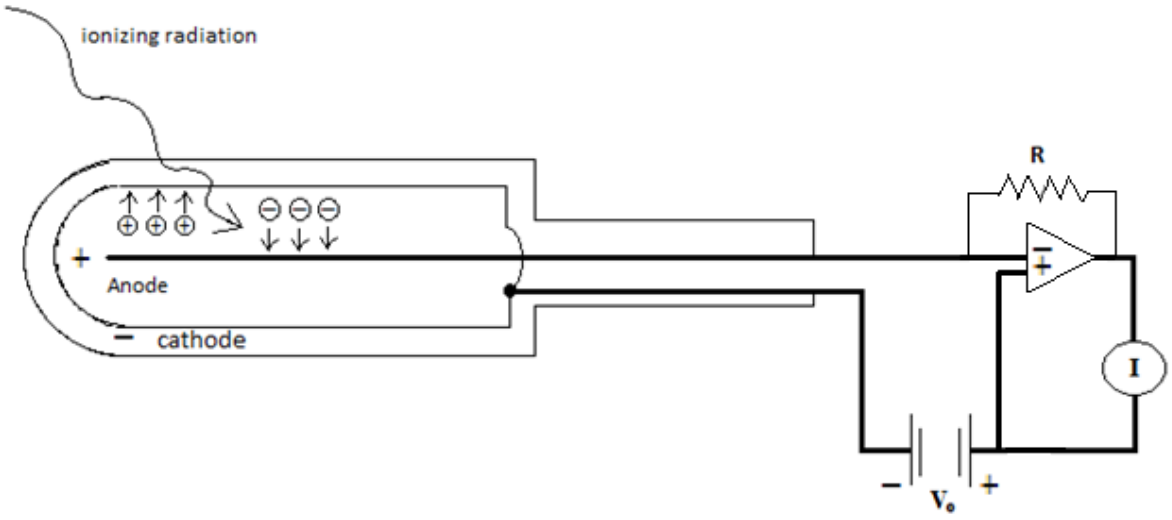

Figure 2. Schematic of an ionization chamber with electrometer in rate mode.

electromagnetic radiation will ionize gas by means of various physical processes. Most commonly, Compton scattering occurs in the gas whereby an x or gamma ray transfers energy to

an atomic electron which is then ejected. Less commonly an atomic electron can gain energy via the photoelectric effect or pair production. Generally, the effective atomic number of the chamber's gas is too low for these processes to be probable. As the positively charged ions and negatively charged electrons are generated they are attracted toward the corresponding electrodes a current is generated in the electrometer attached to the chamber. The total charge liberated from the mass of the gas corresponds to exposure. The exposure, measured in roentgens, is converted to dose by means of a conversion factor determined by an accredited dosimetry calibration laboratory (ADCL) or by comparing the measurement to that of an already calibrated chamber. Used consistently throughout this work, an ionization chamber calibrated at the ADCL facility at the University of Wisconsin was necessary since for the energy ranges used in this work (50 kV-300kV) Bragg-Gray theory does not apply (Ma and Nahum). In addition pressure, temperature, and recombination calibration factors must be applied although many chamber's electrometers correct for these internally. An f – factor (as shown in equation 1.5) must also be applied if dose is being measured in a material other than air. The conversion from exposure to absorbed dose can be written as:

$$Dose\ (cGy) = f_{medium}\left(\frac{cGy}{R}\right) * CF_{temp} * CF_{pres} * CF_{recomb} * CF_{chamber} * X(R)$$

$(Equation\ 1.8)$

1.2.2 Thermoluminescence Dosimeters

One of the most widely used methods of dosimetry, thermoluminescence, has been used for over 60 years. TLDs are relative solid state detectors and are used in myriad applications for determining radiation dose. Materials which exhibit thermoluminescence include calcium fluoride, lithium fluoride, lithium borate, calcium borate and several others. The lattice structure of TLDs allow interactions between atoms and alter the electron energy levels creating a band

structure specific to the type of lattice system a crystal possesses. The band structure describes energy regions where an electron is able to exist; the lowest energy or ground state is known as the valence band, while the uppermost level is called the conduction band. Non-metallic materials such as TLDs possess an energy region or band gap between the valence and conduction band where electron states cannot exist. Impurities intentionally introduced into TLDs cause irregularities in the band structure, allowing electrons to enter the band gap where they can become trapped. Once the TLD is irradiated, electrons are excited into the conduction band and eventually fall back to the ground state. Alternately they can fall into a metastable state brought on by the impurity's traps, where they will remain until they receive sufficient energy, driving them back to the valence band. This transition is accompanied by the emission of a photon with energy equivalent to the difference between the excited and ground states. The light output of the crystal is proportional to the energy initially absorbed from the incident radiation, allowing the exposure to be calculated from the light signal.

A TLD reader is a device which both provides sufficient energy to release trapped electrons as well as generating a signal from the resultant emission of light. The energy provided is in the form of controlled heating during which the light yield is measured. Light yield is measured by photomultiplier tubes (PMTs) which are housed within the so-called "TLD reader" and shielded from all ambient light so that only the output of the TLDs is measured. Light incident on a photocathode within the PMT is converted into electrons via the photoelectric effect; the resulting current is then amplified by a series of dynodes where they can be counted and recorded (in units of nanocoulombs). Typically TLDs require a period of stabilization (usually 24 hours) before they are read. The plot of light yield as a function of temperature is known as a glow curve; an example of which is shown in Figure 3. The total yield can be calculated as the area under the glow curve and subsequently compared to that of other TLDs

calibrated in a known radiation field, which allows one to surmise radiation dose. After this process the TLDs can be exposed to a sequential course of heating, thereby emptying the electron traps and 'erasing' the TLDs so they can be reused.

TLDs used for this work are manufactured by Harshaw and composed of MgTi doped lithium fluoride (LiF:MgTi). Their specifications are summarized in Table 1. The effective atomic number of LiF is similar to that of tissue, allowing the energy absorbed from photons to be matched over a wide range of energies. The reader used for this thesis work was a Harshaw 5500 which uses nitrogen gas to heat TLDs. All TLDs underwent uniformity testing prior to their use; TLDs were exposed simultaneously with an ionization chamber to approximately 1 roentgen by a conventional x-ray unit.

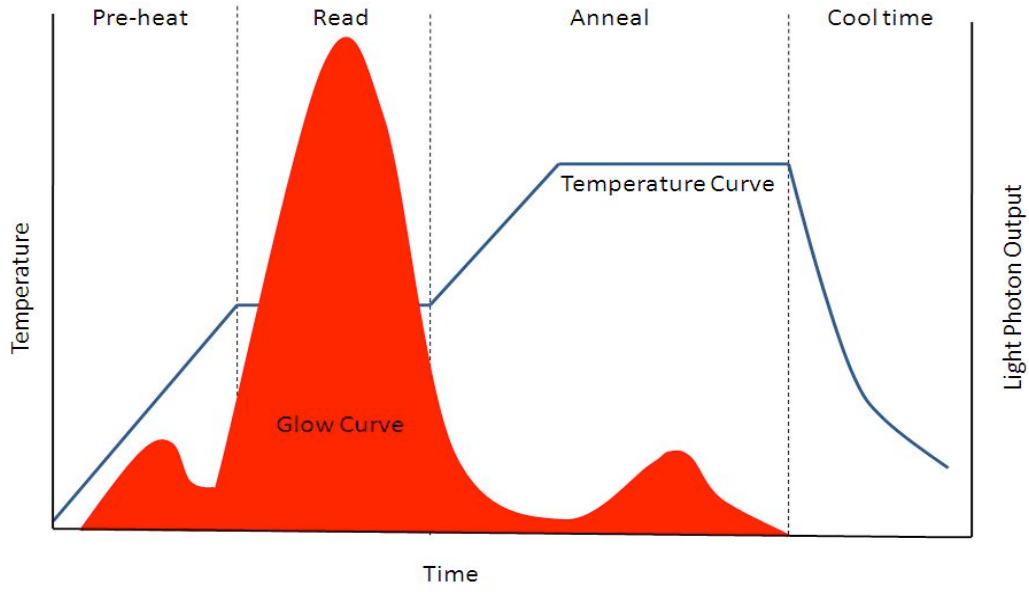

Figure 3. Sample TLD glow curve

The results are then plotted, and those with a result of more than 2 standard deviations from the mean are removed from the batch. Since different batches of TLDs can exhibit different average sensitivities, confirming their precision is crucial to their use in dose measurements.

The process of calibrating TLDs so that useful dose information can be extracted requires that several TLDs are exposed to a known range of doses at a specific energy. Once the calibration TLDs are read, the known dose levels are plotted against their respective background-subtracted readings. The relationship is typically linear, and once the curve is established its slope can be obtained and used as a calibration factor for other TLDs exposed within the dose range of the curve.

Table 1. Harshaw TLD-100 specifications

Material	Lithium Fluoride LiF:MgTi
Size	3.2mm x 3.2mm x 0.9mm
Density	2.64 g/cm^3
Range	10 µGy to 1 Gy linear 1 Gy to 20 Gy supralinear
Threshold	<10 µGy
Energy Range	Photons, > 5 keV Neutron, thermal to 100 MeV Electrons, > 70 keV
Tissue equivalence	Nearly tissue equivalent
Fading	< 20% in 3 months w/o thermal treatment < 5% in 3 months with preheat or glow curve deconvolution
Batch uniformity	±15% Standard deviation from the batch mean
Reuse	More than 500 times per dosimeter with < 10% change in sensitivity

1.2.3 Metal Oxide Semiconducting Field Effect Transistors

MOSFETs, another type of relative solid state detector, have only relatively recently been applied to the field of dosimetry. Conceptually, this form of transistor has been in existence since 1925; it was only after 1974 that the structure was considered as a means of measuring radiation exposure (Knoll). Initially used in a clinical setting to make real time measurements of skin dose for diagnostic radiology and radiotherapy, they have since been validated for use as dosimeters in various other clinical applications (Yoshizumi et al.).

The basic components of a simple MOSFET transistor include metallic electrodes, a silicon dioxide insulator, a silicon substrate of type n or p, and oppositely (n or p) doped regions within the substrate . Figure 4 shows the makeup of a simple MOSFET. The electrodes include a gate, a source and a drain. When a negative voltage is applied to the gate of an n-type transistor, the electrons will migrate away from the insulator while the 'holes' in the p-type doped regions are attracted. This generates a channel for the holes at the top layer of the substrate underneath the silicon dioxide layer. When the MOSFET is exposed to ionizing radiation, electron-hole pairs are created in the silicon dioxide insulator, which drift apart due to the applied voltage from the gate. The electrons' tendency to become trapped in the silicon dioxide-substrate interface causes the voltage between the source and drain to shift negative. In a MOSFET dosimeter the voltage shift is measured as the difference before and after irradiation, and is usually a linear function of the integrated dose. The sensitivity of such a device is increased by applying a greater voltage from the bias supply to the gate, thereby allowing the charge channel to widen increasing the fraction of charge carriers collected (Knoll).

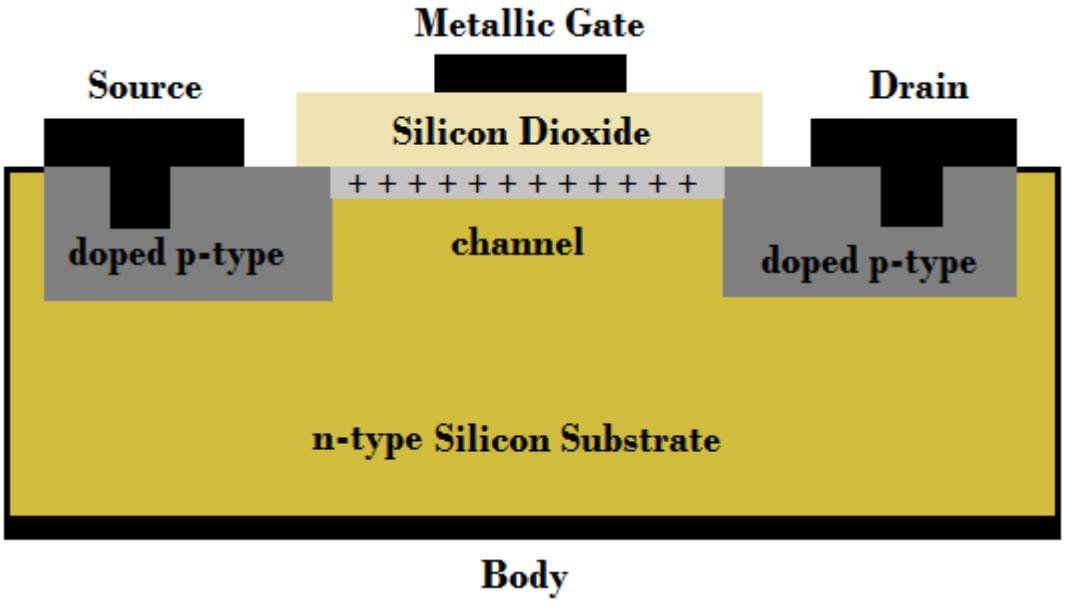

Figure 4. Basic schematic of a MOSFET detector

Being a relative dosimeter, MOSFETs must be calibrated prior to their use. This is done similarly to a TLD with the exception that one expects a linear relationship between threshold voltage and exposure. The dosimeter is exposed to a radiation field simultaneously alongside an ADCL traceable ionization chamber at a specified dose. The calibration factor is calculated as an average of several independent readings in the following manner:

$$CF\left(\frac{mV}{cGy}\right) = \frac{threshold\ voltage\ difference\ (mV)}{ion\ chamber\ reading\ (cGy)} \qquad (Equation\ 1.9)$$

MOSFETs used for this work were produced by Best Medical Canada consisting of an active area of 0.2 mm x 0.2 mm atop a 1mm square chip. They are energy dependent, requiring different calibration factors to be calculated for different beam energies, as well as being dose rate and temperature independent. These MOSFETs are p-type semiconductors with n type doped regions.

1.2.4 Radiochromic Film

The predecessor to radiochromic film (RCF), radiographic film, has been used as an imaging device since the discovery of x-rays. RCF has been developed in the last 4 or 5 decades, and was initially sensitive only to extremely high doses (~10^3 Gy). In the last 20 years it has been progressively improved to be sensitive to doses on the order of 10^{-2} Gy (Brady). RCF is similar to radiographic film in that it is useful as a qualitative 2-D dosimeter. For quantitative measurements they share optical density (OD) as the primary means of estimating dose. This, however, is where their similarities diverge; whereas radiographic film requires a chemical process in order to develop and subsequently measure the OD, RCF does not require a chemical or thermal reaction in order for the darkening of the film to occur. This provides a distinct advantage over previously used dosimetric films, allowing it to be quantified relatively quickly and efficiently. The small size of TLD and MOSFET dosimeters effectively makes them point dosimeters, and as such they are only 1 dimensional. 2-D dosimetry inherently affords higher spatial resolution and allows visualization of high gradient radiation fields (Brady).

OD is used as a measure of the darkening of film resultant from an irradiation. The definition is simply:

$$OD = log\left(\frac{I_0}{I_t}\right) \qquad (Equation\ 1.10)$$

Where I_0 is the incident light intensity and I_t is the transmitted light intensity after it has passed through the film (Khan). While radiographic film requires a chemical process to fix silver bromide molecules that result as ionizing radiation (or visible light) interacts with silver ions, RCF involves a topotactic polymerization reaction. The reaction is a direct result of the kinetic energy released from the incident ionizing radiation per unit mass (Brady). The darkening of the film occurs almost instantaneously as the reaction creates a polymer dye complex within the

active layer of the film (Vitkin). The active layer the film is imbedded on top of a white, opaque polyester layer and underneath a translucent yellow polyester layer, and is insensitive to visible light (Figure 5).

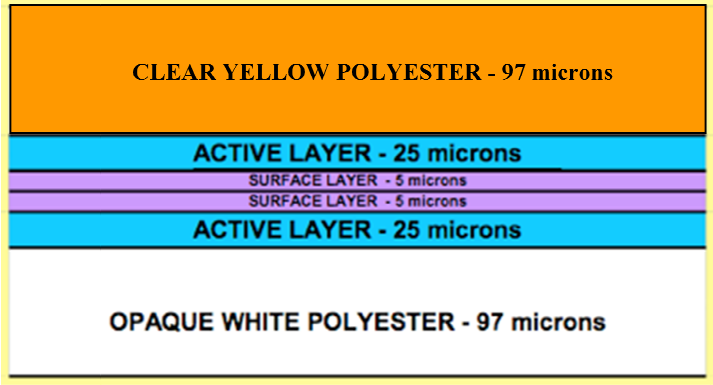

Figure 5. Cross section of GAFCHROMIC® XRQA 2 radiochromic film

GAFCHROMIC® XRQA 2 film was used exclusively for this thesis study. A simple qualitative spatial measurement is possible without any processing whatsoever; however, in order to quantify the dose absorbed by the film, calibration is required. As recommended by the AAPM, after irradiation the film requires 6-12 hours before being read due to a 9% to 11% post exposure OD growth. The digitization is accomplished by using a standard flatbed scanner, in this case an Epson 10000XL. Light is passed through the active layer of the film and the intensity is recorded as a pixel value after it is reflected by the white polyester. After exposure each film is normalized to its unexposed response in order to compensate for manufacturing differences between films. Called net OD, the normalized OD is calculated as follows:

$$net\ OD = OD_{exposed} - OD_{unexposed}$$

$$= \log\left(\frac{I_0}{I_{exposed}}\right) - \log\left(\frac{I_0}{I_{unexposed}}\right) \qquad Equation\ (1.11)$$

$$= \log\left(\frac{I_{unexposed}}{I_{exposed}}\right)$$

where the exposed and unexposed intensities have had the background or "dark field" intensities subtracted (Brady).

Once net OD has been established for a given irradiation, the absorbed dose can be extracted via a calibration process similar to that used for TLDs and MOSFETs. A range of doses is selected based on the expected dose values of the irradiation, and the film is then exposed to these doses alongside an ADCL ionization chamber. The absorbed dose is calculated according to equation 1.8 and this is plotted against the net OD values for each film yielding a calibration curve. The relationship between net OD and absorbed dose is not linear. Brady has determined that the best fit for this relation is an exponential association expressed as:

$$D(net\ OD) = a_1 * (e^{a_2 * net\ OD} - 1) \qquad Equation\ (1.12)$$

Where D(net OD) is the absorbed dose and the coefficients a_1 and a_2 are determined via nonlinear regression (Brady). The equation is then applied to the net OD values for the rest of the experimental films, giving a 2-D dose distribution.

1.3 Anthropomorphic Phantoms

In order to better represent the volumetric scatter conditions of a given exposure, tissue equivalent phantoms were used that simulated actual experimental and clinical conditions. Mouse and rat sized phantoms with uniform density and homogenous medium for small animal

dosimetry studies. Human anthropomorphic phantoms with materials of varying density representing lung, bone, spinal cord, and generic soft tissue were used for clinical studies. All phantoms used in this study were products of Computerized Imaging Reference Systems (CIRS, Norfolk, VA).

The phantom used in the clinical section of this thesis is a CIRS Model 701 ATOM® adult male anthropomorphic phantom. The phantom weighs 73 kg, stands 173 cm high and consists of 38 contiguous sections or slices measuring 25 mm thick. Each slice contains 5mm diameter holes that accommodate point dosimeters such as TLDs or MOSFETs. Each hole has a numbered location inside the region tissue equivalent material within the phantom that represents a particular organ. This configuration allows equivalent dose calculations to be made based on the ICRP weighting factors for the respective organs. The tissue substitute material conforms to the ICRU's definition and the relevant parameters (Table 2) are based on ICRP Report 23 and International Commission on Radiation Units (ICRU) Report 44 specifications.

Table 2. ATOM® male anthropomorphic phantom values for various simulated tissues and the corresponding ICRP or ICRU values.

	Average soft tissue		**Average bone**		**Lung (inhale)**		**Spinal cord**		**Cartilage (vertebral disks)**	
	ICRP 23	CIRS	ICRP 23	CIRS	ICRU 44	CIRS	ICRP 23	CIRS	ICRU 44	CIRS
Density ($g\ cm^{-3}$)	1.03	1.055	1.58	1.6	0.2	0.21	1.038	1.07	1.1	1.155
Z_{eff}	7.23	7.15	11.5	11.5	7.51	7.1	7.41	7.38	7.9	7.87
El. Density ($10^{23}\ cm^{-3}$)	3.42	3.43	5.03	5.03	0.663	0.681	3.45	3.45	3.69	3.7

2. Estimating Effective Dose from Phantom Dose Measurements in Atrial Fibrillation Ablation Procedures

There were three objectives of this study: (1) to determine the effective dose imparted to an anthropomorphic phantom during a typical atrial fibrillation ablation procedure; (2) to relate the effective dose measurements to the dose area product as reported by the console of the fluoroscopy unit operated during an atrial fibrillation ablation procedure; and (3) to make estimations of the cancer risks associated with the procedure. The following sections will provide a more detailed description of these objectives.

2.1 Determination of effective dose according to the ICRP

Since measuring effective dose in an actual patient is untenable, an anthropomorphic phantom must serve as a proxy for these measurements. Traditional TLD measurements are time consuming and labor intensive requiring annealing, post irradiation waiting time, and the reading of the individual dosimeters. MOSFETs have been validated for organ dose measurements and were used to facilitate the measurements for this study (Yoshizumi et al. 2007). The accurate determination of organ doses is essential to ascertain the effective dose imparted to the phantom. The effective dose determination in turn allows the creation of dose conversion coefficients (DCC) and the estimation of cancer risk described in the following two sections. Organ locations are chosen according to how heavily they are weighted in the ICRP 103 algorithm, and their proximity to the radiation field. For example, in AF ablation procedures the beam is positioned over the heart, so lungs are chosen because they are within the field and have the highest tissue weighting factor i.e. 0.12.

2.2 Dose conversion coefficients

Determination of effective dose for an individual patient is impractical. However, modern fluoroscopic units are equipped with flat panel detectors to measure DAP during each procedure. Once ED has been measured in a phantom, it can be related to the measured DAP via dose conversion coefficients (DCCs). Dose conversion coefficients are simply a ratio of ED to DAP and can be used to estimate ED for other AF ablation procedures by multiplying the DCC by the reported DAP. Currently, the majority of DCCs for fluoroscopic procedures are estimated from Monte Carlo simulations (Hart and Wall, Schultz and Zoetelief). These simulations have shown that DCCs can vary based on clinical protocol, beam quality, and body size (Johnson, et al.). Values of DCCs found in the literature can either over- and underestimate effective dose when the simulation parameters do not conform to those of the actual procedures, especially when using a different fluoroscopy system. Experimentally deriving DCCs using anthropomorphic phantoms can more closely match an actual clinical situation, and may be more appropriate for a given machine and a specific institution's protocol (HK Looe et al.).

2.3 Estimating cancer risk in AF ablation procedures

Organ dose measurements can also be utilized to estimate the risk of solid tumors and leukemia in patients who undergo an AF ablation procedure. The estimation of cancer risk is thoroughly detailed in the BEIR VII Phase 2 report, which presents risk models for cancer resulting from any specified dose from low LET ionizing radiation. The models were developed to estimate lifetime attributable risk based on dose, sex, and the age at exposure. While risk models are primarily based on epidemiological studies of the survivors of the atomic bombing of Hiroshima and Nagasaki , BEIR VII Phase 2 also incorporates data for "both medically exposed persons and nuclear workers exposed at relatively low doses". Unfortunately, these risk estimates are subject to myriad uncertainties stemming from inherent epidemiological uncertainty, as well as an

inadequate understanding of the biological effects of low doses of radiation. For solid cancers, estimating the risks from relatively low doses is based on a linear model, whereas the risk estimates for leukemia are based on a linear-quadratic model. Tables are available in BEIR VII that show lifetime attributable risk (LAR) for various cancer sites and for various ages of exposure. The LAR tables have been distilled to show the number of incidences of cancer that can be expected per 100,000 persons exposed to 0.1 Gy. With stochastic effects, the incidence of a given effect is assumed linear with dose, allowing the cancer risk to be scaled according to a given organ's absorbed dose. This makes it relatively simple to generate LAR tables specific to certain patient cohorts once organ doses have been measured. Relative risk (RR) is a way of comparing the incidence of cancer attributable to radiation exposure to the incidence of cancer within an unexposed population. The equation for RR is simply;

$$RR = \frac{(LAR + LR)}{LR} \qquad (Equation\ 1.13)$$

where LR is the lifetime risk of the incidence of cancer for unexposed populations.

2.4 Materials and Methods

No Institutional Review Board approval was required, as this study involved only physical and phantom dosimetry measurements.

2.4.1 X-ray Fluoroscopy System

A male anthropomorphic phantom (model 701-D; CIRS, Norfolk, VA) was used to make organ dose measurements in locations that coincide with the ICRP 103 tissue weighting factors for effective dose calculations. A photograph of the phantom positioned for a typical AF ablation procedure is shown in Figure 6. Detectors were placed in 5mm diameter holes drilled into 38 contiguous slabs with a thickness of 2.5 cm each. The holes correspond to specific organ

locations that are assigned according to the manufacturer's manual. The phantom represents tissue equivalent substitutes with tolerances better than 1% for bone and soft tissue and 3% for lung tissue at photon energies from 30 keV to 20 MeV (9) (Table 2).

Figure 6. Experimental setup of the male anthropomorphic phantom (without MOSFETs) and the Allura Xper FD10/10 biplane fluoroscopy system.

A biplane fluoroscopy system (Allura Xper FD10/10, Philips Medical Systems) was used to expose the phantom. This is the same system used for actual procedures in the electrophysiology laboratory at Duke University Medical Center. This system can automatically vary the tube current and peak voltage during exposures; however, it can be manually set to 'low', 'normal', and 'high fluoro'. Both x-ray tubes, denoted right and left anterior oblique (RAO, LAO respectively), are equipped with flat panel detectors that measure the DAP, which is then reported

on the console as a cumulative (summed) DAP. The relevant parameters for the two settings used in this study are given in Table 3. While the algorithm that determines these parameters is proprietary, the current and energy are generally dependent on the amount of attenuation in the beam and therefore the size of the patient or phantom.

Table 3. Automated fluoroscopy settings used during phantom experiments

	'low fluoro'		'normal fluoro'	
Camera (angle)	RAO (30^{o})	LAO (45^{o})	RAO (30^{o})	LAO (45^{o})
Tube Energy (kVp)	86	93	86	82
Tube Current (mA)	4.8	4.5	12	12.3

2.4.2 Calibration and DAP validation

The MOSFET calibrations and experimental measurements were done using a Philips Allura Xper FD10/10 modified with a 4 cm aluminum plate simulating equivalent human attenuation thickness. The aluminum plate simulated a clinical x-ray tube voltage of approximately 90 peak kilovolts (kVp), allowing the calibrations to take place at the same beam quality as the clinical measurements. MOSFETs were carefully placed at the same level as the active volume of the ionization chamber and exposed three times. The data was read out in millivolts (mV) on a Lenovo® laptop personal computer (PC) and converted to gray. To convert exposure (roentgen) to absorbed dose (Gy), an ADCL chamber specific correction factor for 90 kVp (interpolated between 80 and 120 kVp to be 1.0275 R/rdg) as well as a tissue f-factor (calculated to be 0.94), were applied to the electrometer reading according to equations 1.8 and 1.5. The electrometer

self-corrects for temperature and pressure, so these corrections were not included in the calculations.

The MOSFET AutoSense System (Model TN-RD-60, Best Medical, Ottawa Canada) includes 20 high sensitivity MOSFETs (Model TN-1002RD), a bias supply (Model TN-RD-22), a bias reader (Model TN-RD-21) and AutoSense PC Software (Model TN-RD-45). The MOSFETs were calibrated by simultaneously exposing them along with a 0.6cc ionization chamber (Radcal Model 10x5-6(17624), Monrovia, CA) connected to a Radcal electrometer (Model 9015(91-1205)). Both the chamber and electrometer were calibrated together at the Accredited Dosimetry Calibration Laboratory (ADCL) at the University of Wisconsin, Madison. The Radcal electrometer automatically corrects temperature and pressure.

The mass energy attenuation coefficients (μ_{en}) were obtained by linearly interpolating National Institute for Standards and Technology (NIST) data for soft-tissue (ICRU-44) and dry air near sea level. The absorbed dose measurements were used with the MOSFETs' outputs to create individual calibration factors for all twenty MOSFETs, which were then stored in the PC.

In order to verify the dose area product readout of the fluoroscopy unit a 0.6 cc ionization chamber was inserted between two pieces of polystyrene foam along with a piece of GAFCHROMIC®XR-QA film (ISPCORP, Wayne, NJ) as shown in Figure 7. The foam was cut to accommodate the ionization chamber as well as to ensure that the film was level with the central axis of the chamber. The setup was exposed under a 4 cm aluminum slab and the electrometer reading was again corrected according to the ADCL factor and tissue f-factor described above. The film was then used to estimate the area of the beam at the point of measurement, which was then multiplied by the corrected electrometer reading to give DAP ($mGy\text{-}cm^2$). Since the fluoroscopy unit displays a cumulative DAP from both imagers, the

ionization chamber- film-foam-aluminum configuration was exposed with both imagers separately and the results summed.

2.4.3 Phantom Measurements

The CIRS anthropomorphic phantom was loaded with MOSFETs and exposed under two different fluoroscopy settings 'low' and 'normal'. The fluoroscopy unit's settings are automated in that the tube energy and current are set by the machine, and only 'low', 'normal', and 'high' may be chosen manually (these settings generally double the previous setting's beam current). The high fluoro setting is generally not used clinically due to concerns of overexposure and was therefore not used in this study. Dosimeter locations for the two exposures are listed in Table 4. The skin location was chosen within the beam on the back to serve as an entrance skin dose measurement.

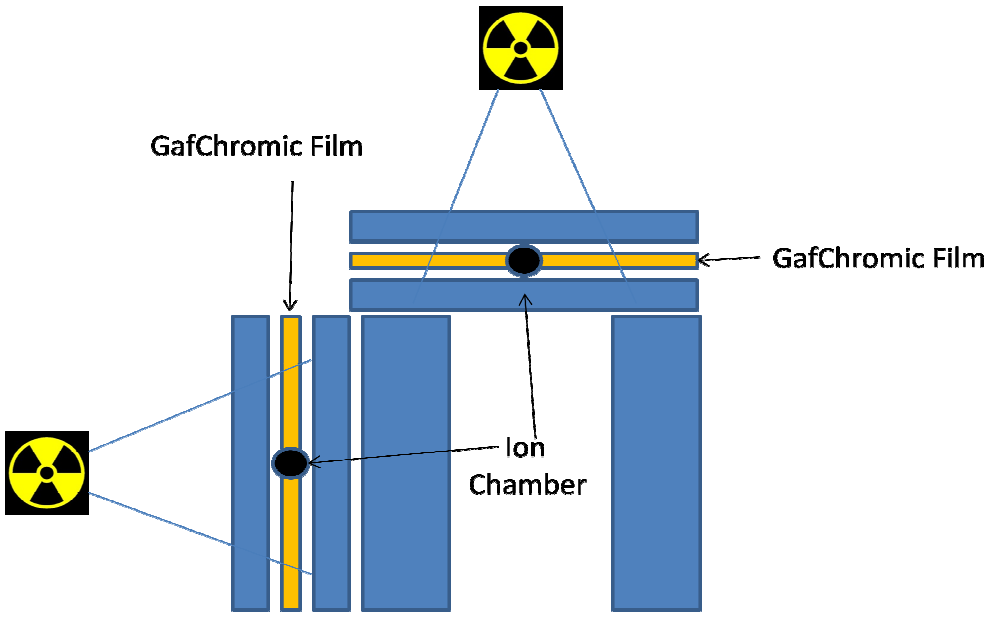

Figure 7. Setup allowing the measurement of DAP in a biplane fluoroscopy unit

Table 4. Organ locations used to calculate effective dose under the two different fluoroscopic settings

'Low Fluoro' Setting		'Normal Fluoro' Setting	
Lens of the eye	Mid Left Lung	Lower Left Lung	Sternum (marrow)
Thyroid	Fourth Left Rib (marrow)	Mid Left Lung (posterior)	Thymus
Upper Left Lung	Breast	Mid Left Lung (anterior)	Breast
Upper Thorasic Spine	Stomach	Upper Left Lung	Stomach (anterior)
Thymus	Liver	Heart wall	Pancreas
Esophagus	Left Kidney	Spleen	Left Kidney
Sternum (marrow)	Pancreas	Stomach (posterior)	Lower Intestine
Lower Lumbar Spine	Lower Intestine	Stomach (anterior)	Bladder
Ovaries (equiv. location)	Bladder	Fourth Left Rib (marrow)	Liver
Testes	Superficial Skin	Esophagus	Superficial Skin

Some of the locations for the 'normal fluoro' exposure were changed, since many of the original locations yielded no measured dose due to their being too distant from the primary beam. The replacement locations were also chosen to give better coverage to more heavily weighted organs in the ICRP 103 formalism. Therefore, two more lung locations were added, one in the lower left lung and another in the mid lung more posterior to the original. Additionally, detectors were added to the heart wall, the spleen, and a second more posterior stomach location.

The phantom was placed in a supine position and the RAO and LAO imagers were positioned by a cardiac electrophysiologist at 30° and 45° respectively, representing the fluoroscopy coverage of a typical atrial fibrillation ablation procedure under biplane mode (Figure 6). The experimental setup was exposed twice for 10 minutes at a time to give an adequately high dose. The MOSFETs were subsequently read along with the DAP and the procedure repeated on the normal setting.

2.4.4 Effective Dose and Conversion Factor Calculations

Effective dose was calculated according to the ICRP 103 formalism. Each organ dose was averaged between the two exposures and then used in equation 1.7 to determine effective dose. The calculated effective dose was then normalized by the total exposure time, yielding an effective dose rate. Similarly the DAP given by the console was averaged for the two exposures and then divided by the exposure time to give a DAP rate. The DCC was simply the effective dose rate divided by the DAP rate. To estimate the effective dose for a typical procedure the effective dose rate was multiplied by the average clinical fluoroscopic time derived from a retrospective review of the electronic records of 79 patients who underwent AF ablation procedures at Duke University Medical Center (DUMC) in 2009. These data are shown in Table 5.

Table 5. Averages and ranges of pertinent information about 2009 DUMC AF ablation patients

	Beam on time (min)	DAP ($Gy\text{-}cm^2$)	Weight (kg)	Age (years)
Average	88.2	276.3	93.7	59.5
Range	36.1-195.0	56-1091	51-154.8	32-78

2.5 Results

Figure 14 and 15 show the individual organ doses as measured by the MOSFETS for the first and second phantom exposures. The effective dose calculated was 27.9 ± 1.7 mSv (range

11.4-61.9 mSv) for the 'low fluoro' setting and 45.6 ± 4.9mSv (range 18.6-101.3 mSv) for the 'normal fluoro' setting, using a mean clinical fluoroscopic time of 88.2 minutes (range 36-195.6 minutes; n=79 patients). For the 'low fluoro' setting an ED/DAP conversion factor of 0.573±0.08 mSv-Gy^{-1}-cm^{-2} was calculated. For the 'normal fluoro' setting the conversion factor was calculated to be 0.577±0.06 mSv-Gy^{-1}-cm^{-2}. While confirming the console's DAP readout, the reported and measured DAP values were 4378 mGy-cm^2 and 4372 mGy-cm^2 respectively, a difference of 0.1% using an arbitrary exposure time of 2 minutes.

The risk calculations based on BEIR VII Phase 2 are shown in Tables 6 and 7. They encompass all age groups seen in patients who underwent AF ablation procedures in 2009, up to age 60.

2.6 Discussions

Literature detailing DCCs for catheter ablation is limited. The United Nations Scientific Committee on the Effects of Atomic Radiation (UNSCEAR) has published data on medical radiation exposure; however, the data comprising radiofrequency ablation is limited and widely varying (Appendix A.1). The United Kingdom's National Radiological Protection Board (NRPB) has reported a value of 0.19 mSv/Gy-cm^2 for radiofrequency ablation procedures based on Hart and Wall's data, which is about 50% of what found in the present study.. The UNSCEAR and NRPB data are based on estimates from Monte Carlo (MC) simulations rather than measured organ doses. In addition, those data were compiled over twenty years ago; fluoroscopy system technology has advanced considerably since that time. Without knowledge of the parameters and geometries of the MC simulations, which are not available in the journal articles referenced by the UNSCEAR and NRPB publications, it is impossible to compare these

studies with the present one. The NCRP also has data published on radiofrequency ablation which gives DCC values ranging from 0.1 to 0.24. Several of these DCCs are derived from the same Hart and Wall paper that the UNSCEAR references.

Table 6. Lifetime attributable risk (LAR) for AF ablation patients based on phantom dose measurements (additional cases per 100,000 exposed).

Age at exposure	30		40		50		60	
Organ	Male	Female	Male	Female	Male	Female	Male	Female
Stomach	2	3	2	3	2	2	1	2
Colon	0	0	0	0	0	0	0	0
Liver	3	2	3	2	3	1	2	1
Lung	144	333	143	330	139	316	122	277
Breast	-	23	-	13	-	6	-	3
Leukemia	111	83	111	82	111	82	109	76

Table 7. Relative risk (RR) for AF ablation patients based on phantom dose measurements.

Age at exposure	30		40		50		60	
Organ	Male	Female	Male	Female	Male	Female	Male	Female
Stomach	1.002	1.004	1.002	1.003	1.001	1.003	1.001	1.003
Colon	1.000	1.000	1.000	1.000	1.000	1.000	1.000	1.000
Liver	1.005	1.006	1.005	1.006	1.005	1.005	1.003	1.004
Lung	1.019	1.062	1.019	1.061	1.018	1.059	1.016	1.051
Breast		1.002		1.001		1.001		1.000
Leukemia	1.134	1.141	1.134	1.139	1.134	1.139	1.131	1.128

A study was performed utilizing phantom measurements to calculate effective dose in AF ablation procedures in 2007(Seguchi et al.). This study showed closer DCC values to those calculated in the present study; 0.41 mSv/Gy-cm^2 calculated by Seguchi et al. compared to 0.57 mSv/Gy-cm^2 in the present work. Several aspects of the study differed from ours. The phantom used for their study was smaller than the one used in the current work, the fluoroscopy system was manufactured by GE as opposed to Philips (as a result the half value layer was only 4.8 compared to 7.8 measured on the Philips system) , and the tube parameters were slightly different due to the automated selections made by either system. Nevertheless, the values were significantly higher than those published by UNSCEAR and NRPB.

There are several limitations of this phantom study. First, due to system limitations only 20 MOSFET detectors could be used simultaneously. While all organs could not be represented, the ICRPs more heavily weighted organs in the area of exposure were covered. The organs that were neglected were those that resided outside the field of the beam and were far enough away from the edge of the primary beam that scatter was negligible. Second, the CIRS phantom is based on ICRP 23's Reference Man. Differences in body size and weight can affect dose measurements and fluoroscopic beam quality (Johnson 2009, Shultz 2005). The effective doses strongly depend on the amount of exposure time, which can vary based on an institution's protocols and complications that may occur during individual procedures. Using DCCs as blanket conversion factors is therefore problematic, in that it cannot yield a reliable measure of the radiation risk to a patient.

In conclusion, anthropomorphic phantom measurements are better suited for studying effective dose for institution-specific protocols and equipment. A dose conversion coefficient of 0.57

mSv/Gy-cm^2 is an appropriate factor for estimating effective dose within this institution, but may lead to overestimations or underestimations of ED elsewhere.

The risks for solid cancers were all reasonably low. Leukemia, on the other hand, presented a more significant risk. This is mostly due to the fact that in adults much of the bone marrow is located in the ribs and sternum, which were well within the primary x-ray beam.

3. MOSFETs in Small Animal Dosimetry Applications

Dose delivery in small animal studies is accomplished primarily using cabinet x-ray or cesium irradiators. Often studies are done and results derived based solely on manufacturers' specifications of the delivered dose, without independent dose verification or an adequate understanding of the machines' capabilities. Many studies involve animal containers or other elaborate geometries not considered by the manufacturers when supplying values for dose rates, isodose curves, or beam quality. Differences between the manufacturer's specifications and the actual absorbed dose delivered in this type of situation can be substantial (Brady, 2009). Accurate dosimetry is especially important when operating in the low dose region where the biological effects of irradiation are poorly understood.

Traditional methods of dosimetry are challenging when dealing with small animals. First, typical ionization chambers are unfeasible for internal dosimetry, due to the large size of the available chambers relative to the size of the rodents typically used in these studies. TLDs can overcome this problem; however, they are highly labor intensive and are difficult to place in vivo. These problems are compounded if multiple techniques and protocols must be examined. MOSFETs can overcome many of these difficulties (Lin). Their miniscule size, prompt readout time, and the ability to be calibrated for multiple energies and measure several locations simultaneously makes them uniquely suited to perform small animal dosimetry.

This study is intended to demonstrate the validity of MOSFETs and tissue equivalent mouse phantoms in the accurate determination of absorbed dose to small animals in cabinet orthovoltage x-ray irradiators. To do so, a systematic comparison with thermoluminescent

dosimeters is established to show concurrence with the current dosimetry standard. New measurements were taken in order to establish more accurate dose rates for various beam qualities in order to improve upon the dose rates measured by Abogunde. The major improvement over previous work is a direct result of obtaining ADCL calibration factors for higher energies from the University of Whiscons. The results of a Bland-Altman analysis further indicate that both TLD and MOSFET measurements are in agreement, as indicated by the difference between the two measurements falling within 1.96 standard deviations of the mean. Dose profiles are also generated with radiochromic film and compared to MOSFET measurements to show that the dose received by the phantom and (by proxy) the mouse are nonuniform due to tissue attenuation.

3.1 Materials and Methods

3.1.1 Orthovoltage X-ray Irradiator

The AGFA XRAD-320 Orthovoltage X-ray unit (AGFA NDT Pantak Seifert GmbH & Co. KG, Ahrensburg, Germany) housed in the Edwin A. Sands Building on Duke University's campus is primarily used to provide a predetermined dose of radiation to small animals and cell cultures. Entirely self-contained, it has a 4000 pound steel-lead-steel layered construction that prevents leakage above 0.5 mR/hr at the unit's external surface. The interior cabinet dimensions are 102 x 75 x 86 cm, with an adjustable shelf, a collimator which includes light field indicating the size of the field of view of the beam, and several interchangeable filters for altering the beam quality. The ISOVOLT HS X-ray tube houses the cathode and anode generators used to excite the x-ray filament, an oil cooler, and an operating console that allows tuning of the tube current, voltage, and irradiation time. The maximum tube potential and current are 320 kV and 10 mA respectively and can be adjusted as low as 50 kV and 2 mA. The tube itself is mounted to the cabinet ceiling, giving a source to target distance of 72 cm to the base of the cabinet.

The X-ray tube produces a beam of electrons accelerated from the cathode to the tungsten anode after the cathode filament is heated by a separate power supply. Electrons are emitted from the cathode after it has reached approximately 2000^{o}C and are attracted to the anode. The tube current is varied primarily by adjusting the filament temperature. The electrons interact with the tungsten anode during which a small fraction of their energy is converted to photons through bremsstrahlung and characteristic x-ray processes. These photons subsequently irradiate the target medium. Extensive research has gone into characterizing the XRAD-320's beam quality, which is shown to have a half value layer of 1.117 mm Cu with filter 1 in place and 1.422 with filter 4 (Abogunde).

3.1.2 Dosimeters

TLDs used in this study are TLD-100 lithium fluoride dosimeters (Harshaw), the characteristics of which can be found in Table 1. They were annealed by heating at 400° C for 1 hour then cooled to 100° C for 2 hours. The readout was done by a Harshaw TLD 5500 (Thermo electron corporation) after the TLDs were left to rest in darkness for 24 hours.

The mobile MOSFET Dose Verification System (Model TN-RD-70-W, Best Medical, Ottawa Canada) used for this work includes a Mobile MOSFET bias supply (TN-RD-38), wireless transceiver (TN-RD-16), and five high sensitivity MOSFET detectors (TN-1002RD). A notebook computer was used to collect data for calibrations and dose measurements, which were exported to an Excel® spreadsheet on site.

GafChromic XR-QA radiochromic film (International Specialty Products) was used to obtain attenuation and dose distribution data by cutting the film and inserting it into a 2 cm diameter water phantom constructed from a plastic vial. The phantom was positioned so that the film was vertical and parallel with the center of the x-ray beam. The optical density information

was obtained by scanning the exposed film with an Expression 10000XL scanner (Epson). Calibration data was then applied to the optical density measurements to provide dose distributions.

3.1.3 Rodent Phantoms

Two types of tissue equivalent phantoms manufactured by CIRS were utilized to make dose assessments for the irradiators: a 2 cm diameter, 8 cm long "mouse" phantom and a 3 cm diameter, 12 cm long "rat" phantom. Both phantoms have holes 5 mm in diameter perpendicular to their long axes used to place detectors; two in the mouse and three in the rat. Figure 8 shows a diagram of the mouse phantom. The tissue equivalent material is homogenous with a density of 1.055 g cm^{-3} and an effective atomic number of 7.15, conforming to the ICRU's definition of a tissue equivalent substitute. MOSFET measurements were made by placing two detectors inside

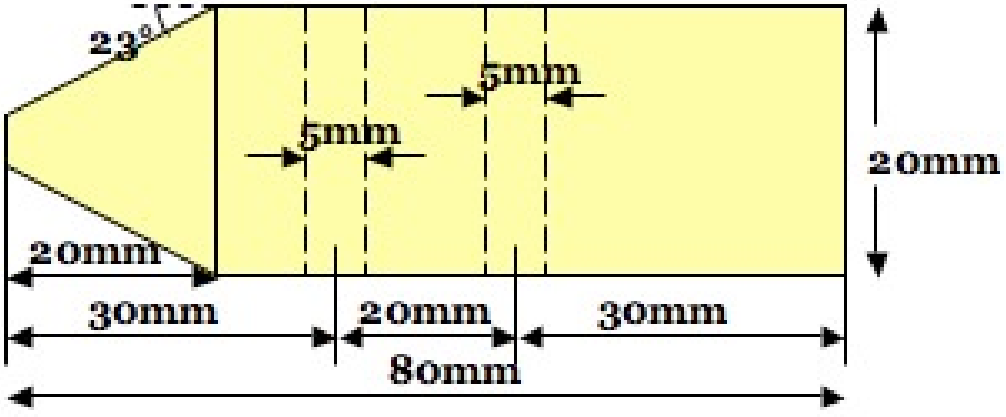

the

Figure 8. Diagram of the CIRS Tissue Equivalent Mouse Phantom

mouse phantom (three in the rat), one dorsally on the surface, and one ventrally. All detectors were positioned perpendicularly to the beam with the phantom centered in the x-ray field.

Three exposures were made at 250 kVp for 72 seconds each and averaged. A similar approach was used with the TLDs at the same settings, with the exception that 2 TLDs were placed inside each hole and on the surface of the phantoms and exposed once. Each configuration was used with the F1 filter as well as the F4 filter to provide data for different beam qualities.

3.1.4 Calibrations

All irradiations for this work were done with the Xrad 320 orthovoltage x-ray irradiator (Precision X-ray Inc) at a source to detector distance of 50 cm and a 10 x 10 cm field of view. The TLDs, MOSFETs, and GaFChromic Film were all calibrated using an 0.18cc ionization chamber (Radcal Model 10x5-.018, Monrovia, CA) and the Radcal electrometer (Model 9015). Both were calibrated simultaneously by the Accredited Dosimetry Calibration Laboratory (ADCL) at the University of Wisconsin, Madison. For the purposes of this work all calibrations and subsequent exposures were done at 250 kVp to match the ADCL calibration energy of the ionization chamber. To convert exposure into absorbed dose, the electrometer reading was corrected using the chamber and energy specific ADCL correction factor of 1.028 R/reading ,as well as the tissue f factor of 0.96 according to equation 1.8. TLDs and MOSFETs were calibrated as described in sections 1.2.2 and 1.2.3 respectively. All three dosimeters (GaFChromic Film, MOSFETs, TLDs) were calibrated in the same instance by placing five high sensitivity MOSFETs, one square piece of film (approximately 6.25 cm^2) and two TLD chips adjacent to the ionization chamber, then exposing them to a range of doses encompassing the target doses for all subsequent exposures . All dosimeters were aligned with the center of the active volume of the ionization chamber using carefully cut blocks of foam to limit backscatter from the irradiator's table top. Separate calibrations were done for both F1 and F4 filters to account for the difference in beam quality.

Calibration factors for the MOSFETs were obtained by dividing the corrected ionization chamber reading by the individual detector responses (equation 1.9) and then averaging all exposures to yield 5 detector specific factors. For each run two TLDs from each batch were exposed and compared with the ionization chamber readings. TLDs responses were read in Coulombs (C) and averaged after subtracting the background readings then plotted against the corrected ionization chamber readings (cGy) and fit with a linear curve. The curve's slope was then used as a conversion factor for the TLDs (Appendix C). The radiochromic film was calibrated by cutting six squares of the film and exposing individual cuttings simultaneously with an ionization chamber to doses ranging from 1 – 200 cGy. The optical densities recorded for each cutting was matched with its respective ionization chamber reading and fit to a curve commensurate with equation 1.12. This calibration curve was then applied to subsequent measurements using a MATLAB code based on work done by Brady to produce dose distribution maps.

3.1.5 Measurements

To compare the TLD and MOSFET detectors in a typical phantom measurement the phantom was placed in a 10 x 10 cm field at a source to detector distance of 50 cm. For the mouse phantom, two TLDs were placed into each hole, while two were left on the surface of the phantom. This arrangement was exposed twice for 1.2 min with filter F1 and 1.4 min with filter F4. Similarly, MOSFETs were inserted into each hole with one on the surface and then exposed three separate times for 1.2 minutes using filter F1, and for 1.4 minutes using filter F4. The phantom was positioned so that the axis of the holes was perpendicular to the beam axis in order to avoid any attenuation from the MOSFET's cables. All exposures were done at 250 kVp and 10 mA. The same arrangement was used with the rat phantom, except that an additional dosimeter was placed into the extra hole in the larger phantom. The raw data was then subjected to appropriate calibration and correction factors described above and averaged for each location.

In order to provide further validation of the MOSFET's measurements and more clearly compare them to those of the TLDs, the two detectors were simultaneously irradiated. A 250 kVp beam was used with a current of 10 mA at a source to detector distance of 50 cm to expose the detectors in air for various times to achieve six dose levels. The measurements were done in the presence of the ionization chamber, which was used as a gold standard for the analysis. After having correction and calibration factors applied, the MOSFET and TLD values were averaged. A Bland-Altman Plot was created by taking the difference in the two measurements for each dose level and plotting it against the average of the two measurements. Limits of agreement are calculated by taking 1.96 standard deviations of the difference (Bland and Altman). Attenuation data was collected for the tissue equivalent phantoms by configuring the MOSFETs such that one was placed on the top surface one inside and one underneath the smaller phantom.

To better simulate actual in vivo measurements, a mouse carcass was selected that closely approximated the dimensions of the phantom. MOSFETs were placed at equal source to detector distances as in the phantom. Radiochromic film was used to make continuous attenuation measurements inside the water phantom described in the Methods section. All of these measurements were taken for a 10 X 10 cm, 250 kVp beam with a current of 10 mA at both beam qualities.

3.2 Results and Discussion

Summarized in Figure 9, the phantom measurements indicate good agreement between MOSFET and TLD. All dose values corresponding to the same position fall within the margins of error. A comparison of the two detectors with the ADCL calibrated ionization chamber is shown in Figure 10. As indicated in the graph, the highest difference calculated is 7% for the TLDs and 2.5 % for the MOSFETs. The higher difference seen in the TLD measurements is likely due to the typical inter-batch nonuniformities which can be as high as 15% (see Table 1). The percent difference

between the ionization chamber's and both detector's measurements gives a good indication that MOSFETs as well as TLDs are comparable to the gold standard ADCL calibrated ionization chamber and are appropriate for dose measurements in small animals.

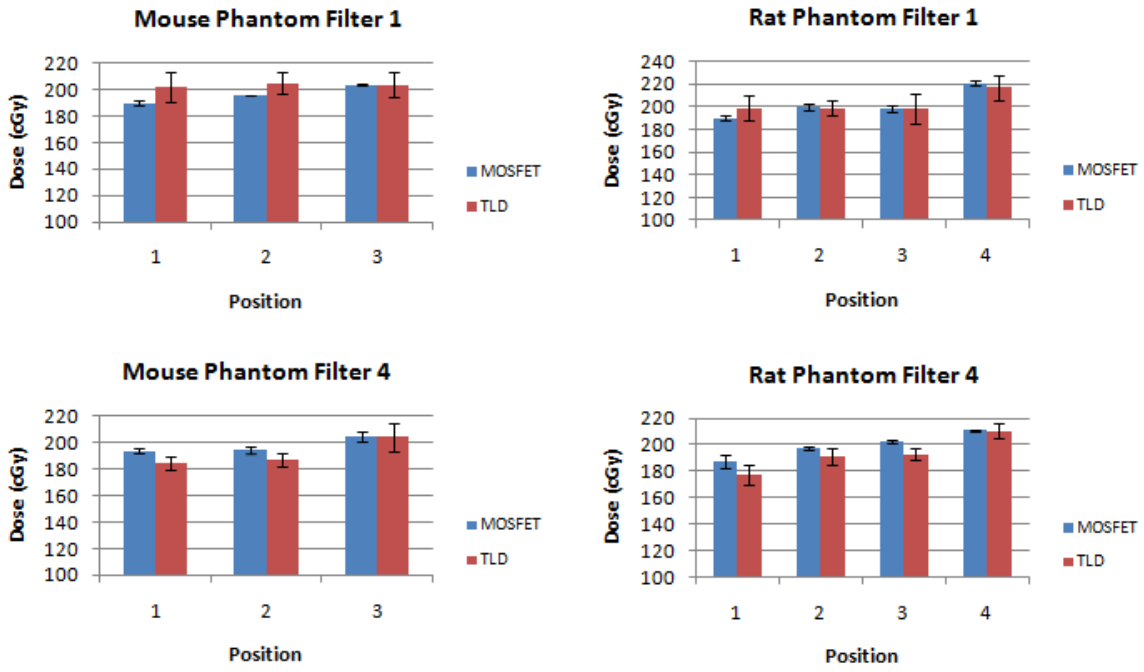

Figure 9. Dose value comparison between Mouse and Rat Phantoms with Filters 1 and 4 as measured with TLDs and MOSFETs.

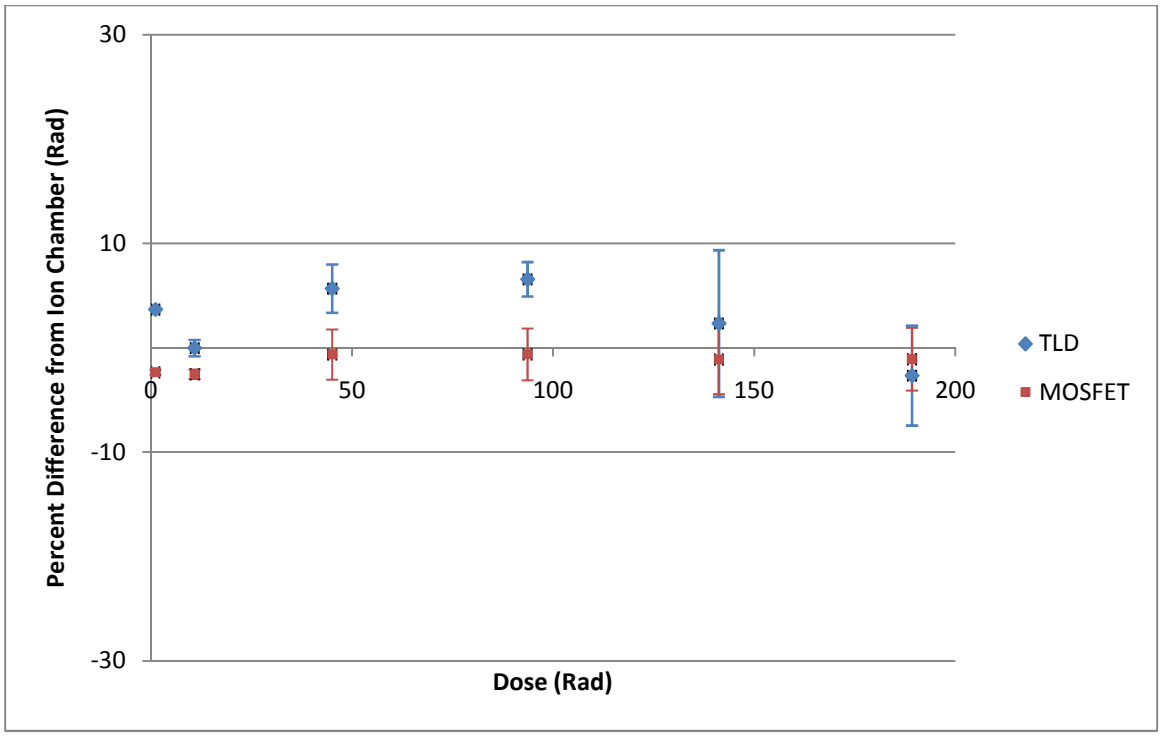

Figure 10. MOSFET and TLD percent difference from ADCL ionization chamber free in air

A Bland-Altman plot was created from the same data to show the correlation between the two methods of measurement. Figure 11 gives the difference between the TLD and MOSFET measurements plotted against the average value of the two. The limits of agreement are indicated by the dotted lines and were computed as the bias or average difference ± 1.96 times the standard deviation of the difference. The measurements fall within that range and as such indicate comparability between the two methods of measurement. This data provides strong evidence that MOSFETs are valid tools for accurately determining the absorbed dose to small animals in an orthovoltage irradiator and provide results comparable to TLDs.

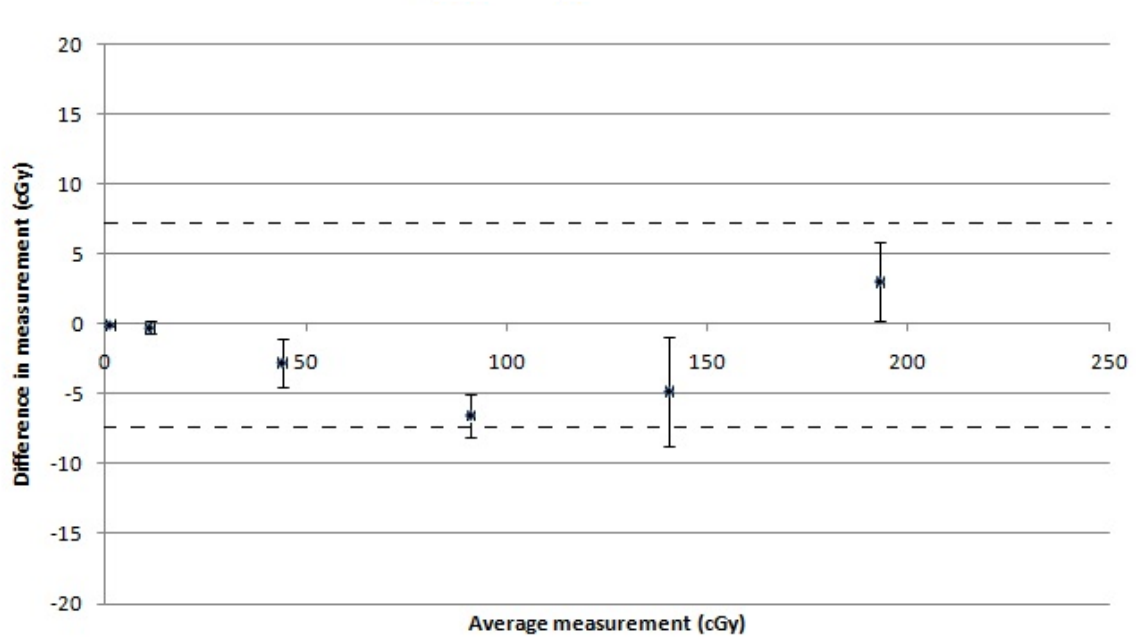

Figure 11. Bland-Altman Plot comparing TLD and MOSFET Detectors in Free Air in XRAD-320 Irradiator

Phantom as well as in vivo MOSFET data also indicate that within small animal targets the x-ray beam is significantly attenuated. This is most pronounced in the rat phantom, which is to be expected due to its larger size. Beam hardening can be achieved with the copper filter (filter F4) but attenuation still persists. Figure 12 shows attenuation in the mouse carcass as well as in the CIRS phantom for filter F1. Radiochromic film provides a much better visual indication of the non-uniformity of the dose distribution Figure 13. This is problematic, particularly for radiation biology studies where results are often reported as a uniform exposure to an animal. It is apparent that the phantom doses are not uniform and as such could cause erroneous conclusions. The solution could be to irradiate animals in a higher energy irradiator such as a Cesium or Cobalt unit, or to irradiate with dual opposing beams. The latter could be achieved with a single by

placing an animal on its back during half of the irradiation, this however is quite challenging when dealing with live, conscious animals.

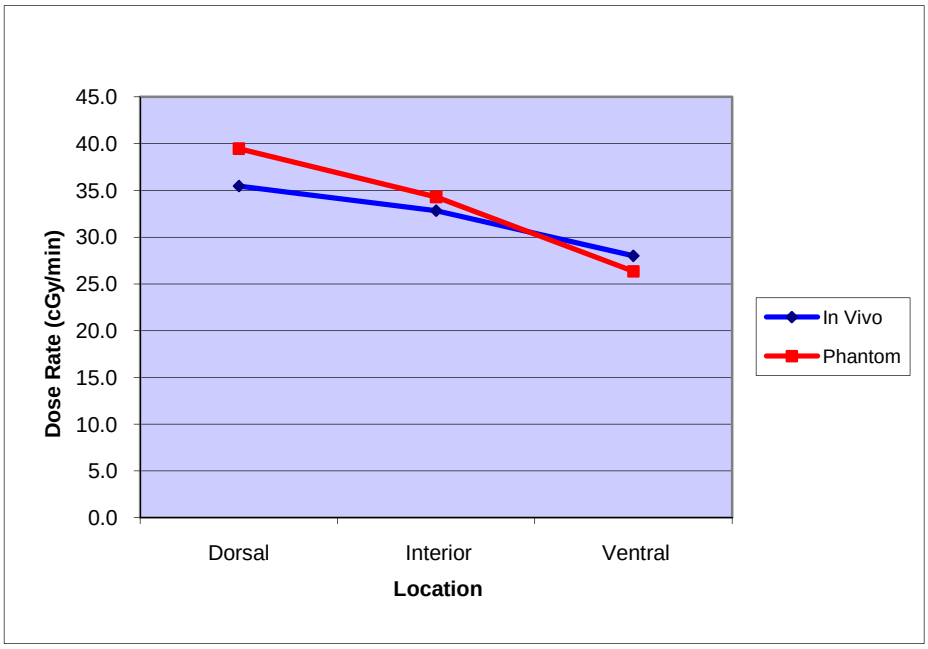

Figure 12. Dose attenuation in the CIRS phantom as compared with that in vivo in the XRAD-320 irradiator with filter F1

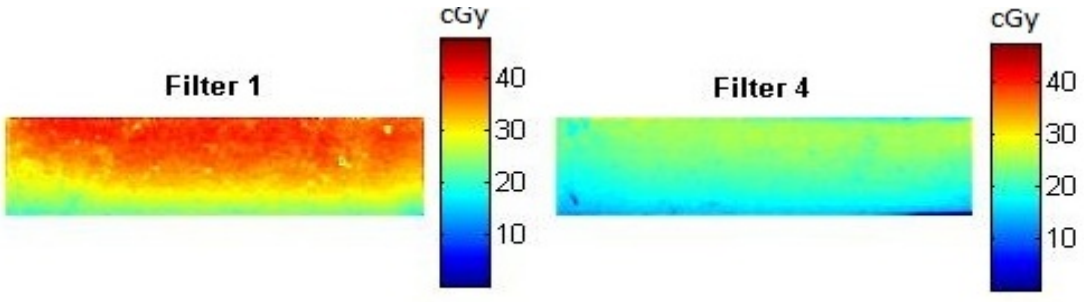

Figure 13. Dose attenuation as seen in a water phantom irradiated with filters F1 and F4

Appendix A. UNSCEAR and NCRP Fluoroscopic Data for Radiofrequency Ablation Procedures

A.1 UNSCEAR Radiofrequency Ablation Fluoroscopy Data

Table 8. Fluoro Time, Skin Dose, DAP and ED data for Radiofrequency Ablation Procedures from the UNSCEAR

Fluoroscopy time (min)	Localized Dose To Skin (Gy)	Dose Area Product ($Gy*cm^2$)	Effective Dose (ED) (mSv)
42 (27108)	-	116	-
50 (31 SD)	-	-	17
21.4 (142 max.)	0.9 (6.2 max.)	-	-
(190 max.)	(8.4 max.)	-	-
28 (3109)	-	103	-
-	0.07 (1.4 max.)	-	-
-	-	56.4 *g*	-
-	-	77.5 *h*	-
-	-	97.3 *i*	-
53 (± 50)	1.3 (± 1.3)	-	17 / 25 *j*
-	0.93 (± 0.62)	-	-
65 (5195)	1.0 (0.083.1)	-	-
28.9	-	91.1	17.3
-	-	43.6	-

A.2 NCRP Radiofrequency Ablation Fluoroscopy Data

Table 9. KERMA-Air product, DCCs, and ED data from the NCRP

Kerma-Area Product ($Gy\text{-}cm^2$)	Dose Conversion Coefficient (DCC) ($mSv/Gy\text{-}cm^2$)	Effective Dose (mSv)
30	0.1	3
	.14	
		21
		17.3
	0.18-0.2	
	0.21-0.23	
33.1	0.19	6.3
48.7		15.2
6.4-230		2.1-59.6

Appendix B. Specific Organ Doses for an Average AF Ablation Procedure at DUMC

B.1 'Low Fluoro' Setting

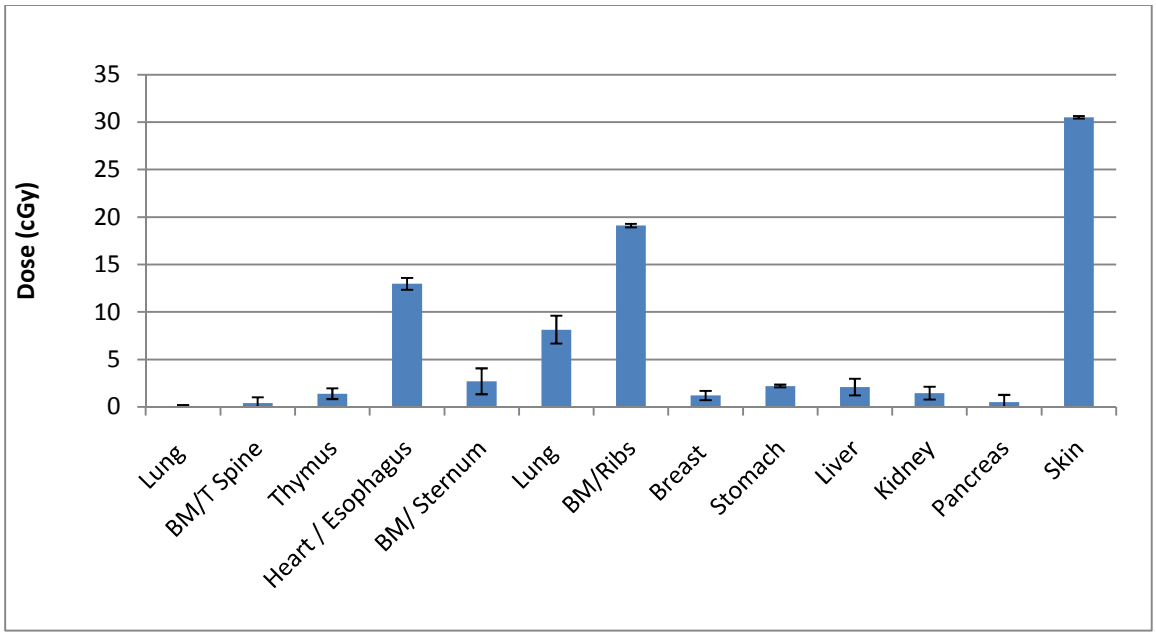

Figure 14. Phantom Organ Doses for 88.2 Minutes of 'Low Fluoro'

B.2 ‘Normal Fluoro’ Setting

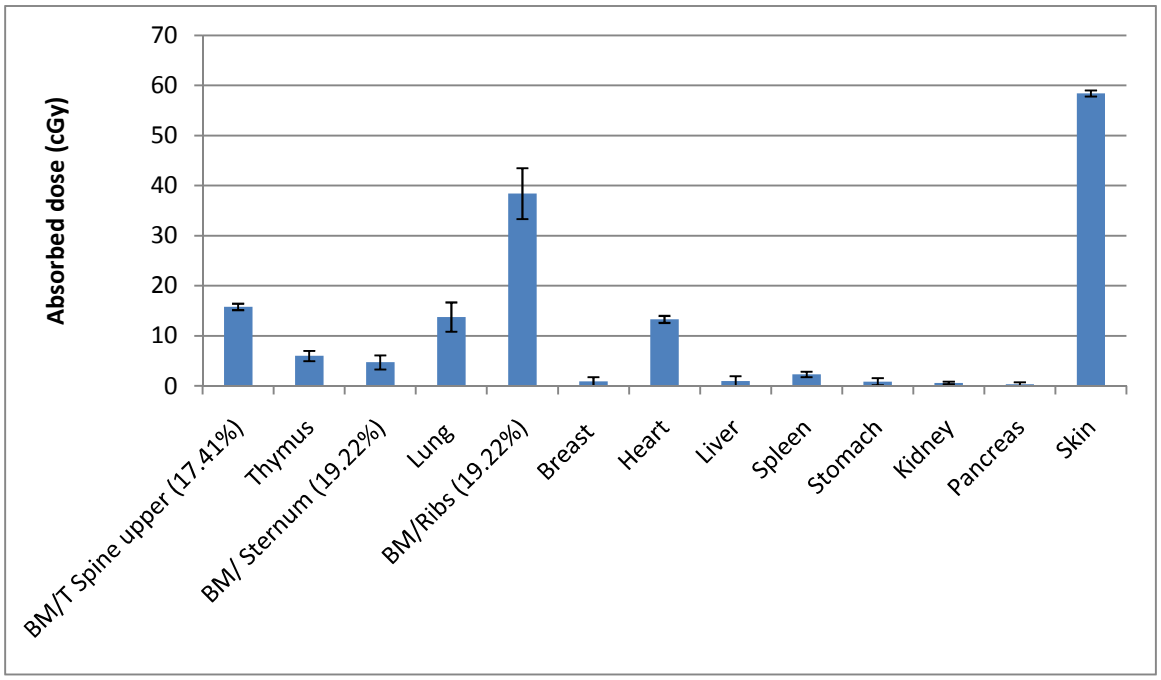

Figure 15. Phantom Organ Doses for 88.2 minutes of 'Normal Fluoro'

Appendix C. TLD Calibration Curves used in TLD-MOSFET Validation Study.

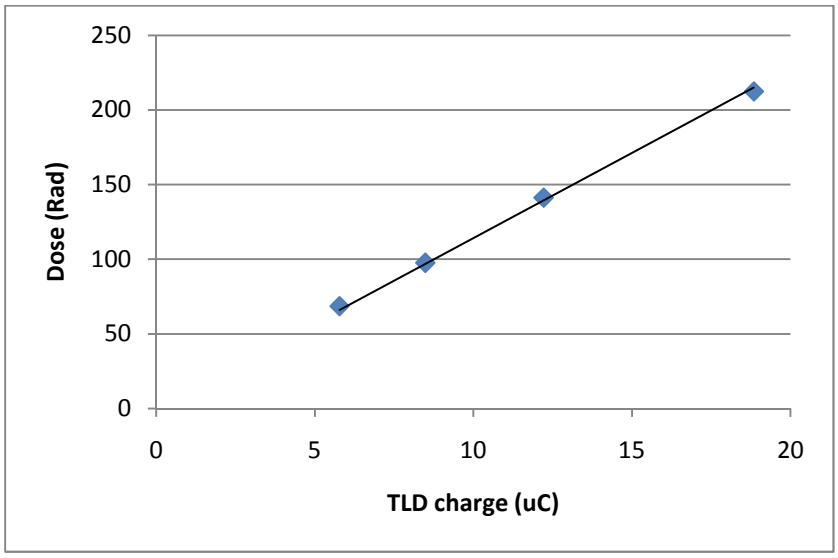

Figure 16. TLD Batch 6 Calibration Curve

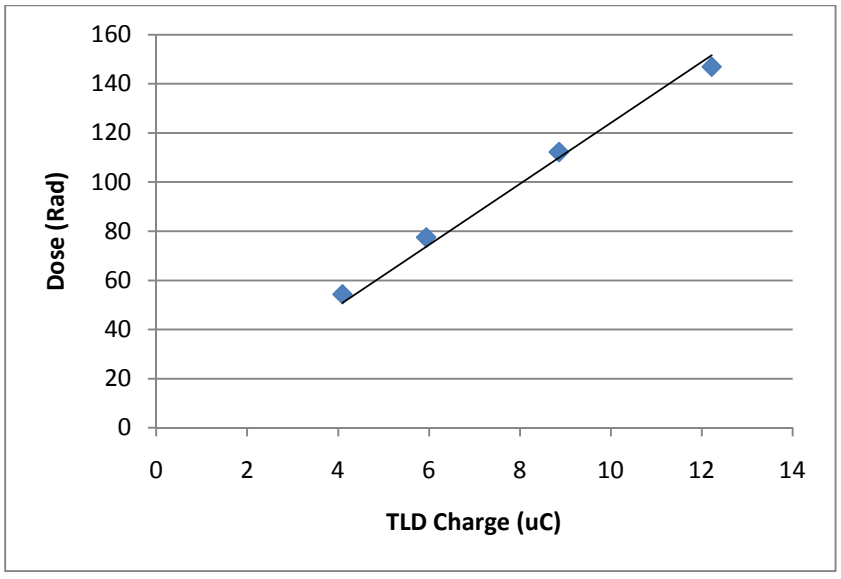

Figure 17. TLD Batch 7 Calibration Curve

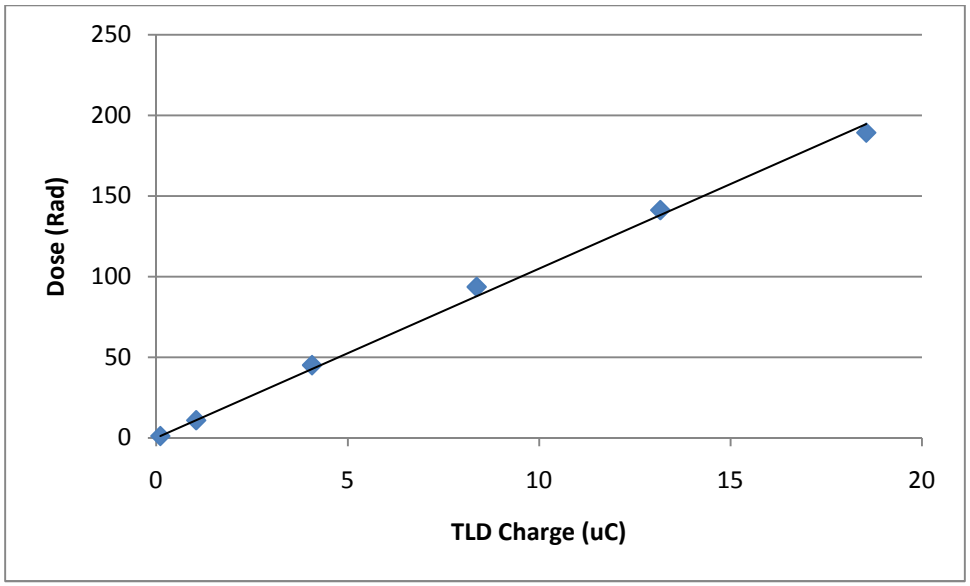

Figure 18. TLD Batch 11 Calibration Curve

References

ATOM Adult Male Phantom User Manual, CIRS, Norfolk, VA.

Attix, Frank. *Introduction to Radiological Physics and Radiation Dosimetry*. Wiley-Interscience, 1986.

Bland JM, Altman DG. Statistical methods for assessing agreement between two methods of clinical measurement. Lancet 1 (1986): 307-10.

Brady, Sameul L. Development of Radiochromic Film for Spatially Quantitative Dosimetric Analysis of Indirect Ionizing Radiation Fields. Ann Arbor, MI: UMI Dissertation Publishing, 2010.

Brady SL, Toncheva G, Dewhirst MW, and Yoshizumi TT. Characterization of a 137Cs Irradiator from a New Perspective with Modern Dosimetric Tools. Health Physics Journal 2009, 97: 195-205.

Cheung, T.; Butson, M.J. Post-irradiation colouration of Gafchromic EBT radiochromic film. Physics in Medicine & Biology 50(2005): 281-285.

Committee to Assess Health Risks from Exposure to Low Levels of Ionizing Radiation, National Research Council. Health risks from exposure to low levels of ionizing radiation: BEIR VII phase 2. Washington, DC: National Academies, 2006.

Fuster V et al AHA/ACC Guidelines Management AF. *Circulation* 2006; 114: e257-e354.

H. K. Looe, F. Eenboom, et al. Conversion coefficients for the estimation of effective doses in intraoral and panoramic dental radiology from dose-area product values. *Radiation Protection Dosimetry* (2008) 131 (3): 365-373.

Hart D, Wall BF. Radiation exposure of the UK population from medical and dental x-ray examinations. Chilton, UK: National Radiological Protection Board, 2002. Publication no. NRPB-W4

International Commission on Radiological Protection. ICRP publication 103: Recommendations of the ICRP. Elsevier. Feb 2008 Annals of the ICRP volume 37/2-4

Johnson P, Lee C, Johnson K, et al. The influence of patient size on dose conversion coefficients: a hybrid phantom study for adult cardiac catheterization. *Phys Med Biol*. 2009 Jun 21; 54(12):3613-29

Khan, Faiz M. *The Physics of Radiation Therapy.* 3rd. Minneapolis, MN: Lippincott Williams & Wilkins, 2003.

Knoll, Glenn F. Radiation Detection and Measurement Third Edition, John Wiley & Sons, Inc. 2000.

Lin, MD, Toncheva G, Nguyen G, Kim S, Anderson-Evans C, Johnson GA, and Yoshizumi. TT. Application of MOSFET Detectors for Dosimetry in Small Animal Radiography Using Short Exposure Times. Radiation Research 2008 ; 170: 260-263.

Ma,C.-M., and A.E. Nahum. (1991). Bragg-Gray theory and ion chamber dosimetry in photon beams. Phys Med Biol 36: 413-428.

NCRP publication 106. Ionizing Radiation Exposure of the Population of the United States. 2009

Rink, I.A. Vitkin and D.A. Jaffray, " Suitabiltiy of radiochromic medium for real-time optical measurements of ionizing radiation dose," Med Phys 32, 1140-1155 (2005).

Schultz FW, Zoetelief J. Dose conversion coefficients for interventional procedures. *Radiat Prot Dosimetry*2005; 117:225 –230

Seguchi S, Aoyama T, Koyama T, et al. Evaluation of exposure dose to patients undergoing catheter ablation procedures—a phantom study. Eur Radiology (2008) 18: 2559-2567.

United Nations Scientific Committee on the Effects of Atomic Radiation. Report to the General Assembly: sources and effects of ionizing radiation. New York, NY: United Nations Scientific Committee on the Effects of Atomic Radiation, 2000

Yoshizumi TT, Goodman PC, Frush DP, et al. Validation of metal oxide semiconductor field effect transistor technology for organ dose assessment during CT: comparison with thermoluminescent dosimetry. *AJR* 2007; 188:1332 –1336

Yoshizumi TT, Sarder M, Goodman PC, Frush DP, Barnes L, Nguyen G. "Application of MOSFET technology in CT organ dose assessment." *Med Phys* 30(2003):1422